

Optimization of the microstructure and properties of Co-substituted Fe–Si–B–Nb–Cu nanocrystalline soft magnetic alloys

M. Ohnuma,^{a)} D. H. Ping, T. Abe, H. Onodera, and K. Hono
National Institute for Materials Science, 1-2-1 Sengen, Tsukuba 305-0047, Japan

Y. Yoshizawa
Advanced Electronics Research Laboratory, Hitachi Metals, Ltd., 5200 Mikajiri, Kumagaya 360-0843, Japan

(Received 23 August 2003; accepted 28 February 2003)

The effect of Co replacement for Fe on the microstructure and soft magnetic properties of $\text{Fe}_{78.8-x}\text{Co}_x\text{Nb}_{2.6}\text{Si}_9\text{B}_9\text{Cu}_{0.6}$ ($x=5-60$) nanocrystalline alloys has been studied for improving the soft magnetic properties of Fe–Si–B–Nb–Cu type alloys at a high frequency range. The magnetic anisotropy constant increases with x , but the coercivity increases when x exceeds 20, indicating that magnetic softness is degraded by replacing Fe with Co. Three-dimensional atom-probe observations have revealed that the number density of Cu-enriched clusters decreases with x , thereby decreasing the number density of the heterogeneous nucleation sites for bcc-Fe primary crystals. In addition, differential scanning calorimetry measurements show that the Cu clustering temperature shifts to a higher temperature with increasing x , suggesting that the kinetics for the Cu clustering decreases as Co content. These experimental results are discussed from the thermodynamical point of view, and the optimized Cu composition to achieve a low coercivity with 40 at % Co has been found. © 2003 American Institute of Physics. [DOI: 10.1063/1.1569396]

I. INTRODUCTION

The development of nanocrystalline Fe–Si–B–Nb–Cu alloys, commercially known as FINEMET, established a new approach to develop soft-magnetic materials with high magnetic flux density, that is magnetocrystalline anisotropy can be reduced by refining the grain size in less than a few tens of nanometers.¹ This experimental finding was later explained by Herzer using the “random anisotropy model.”² The nanocrystalline microstructure of FINEMET is produced by crystallizing an amorphous precursor, the mechanism of which has been extensively studied by transmission electron microscopy (TEM),³ atom-probe field ion microscopy (APFIM),^{3–5} extended x-ray absorption fine structure (EXAFS),^{6,7} differential scanning calorimetry (DSC),^{8–10} small-angle neutron scattering (SANS),^{9–12} and Mössbauer spectroscopy.^{8,13} From these results, it is now widely accepted that the following two factors cause the formation of the nanocrystalline microstructure of the FINEMET type alloys; (1) Cu clustering in the amorphous precursor provides a large number density of heterogeneous nucleation sites for bcc-Fe(Si) primary crystals, and (2) the growth of the primary crystals is controlled by the volume diffusion of solute elements. A recent three-dimensional atom-probe (3DAP) study⁵ confirmed that Cu clustering occurs before the crystallization of bcc-Fe(Si) and that almost all of the primary crystals are nucleated in direct contact with the Cu clusters. A small and broad exothermic reaction corresponding to the Cu clustering was observed by recent DSC measurements.^{9,10} The clustering temperature becomes lower

with increasing Cu content because the supersaturation of Cu in the amorphous phase increases. The clustering temperature also shows a strong heating rate dependence, and it was found that the interplay between the kinetics of Cu clustering and crystallization influences the final microstructure significantly. A similar effect of Cu addition was found in other Fe-based soft and hard nanocrystalline magnetic materials such as $\text{Fe}_{88}\text{Zr}_7\text{B}_4\text{Cu}_1$ (Ref. 14) and $\text{Fe}_{75.8}\text{Nd}_{4.5}\text{B}_{18.5}\text{Cu}_{0.2}\text{Nb}_1$.¹⁵

Continuing efforts to improve the soft magnetic properties of FINEMET alloy have been made by modifying the alloy compositions. Müller *et al.*¹⁶ reported that the substitution of Fe by Co decreases the saturation magnetostriction in FINEMET type amorphous alloys. Adding Co is also expected to be beneficial to induce in-plane magnetic anisotropy to ribbons by magnetic field annealing, because the substitution of Fe with Co is known to be effective for increasing the magnetic anisotropy constant, K_u , of Fe–Si–B amorphous alloys.¹⁷ A large K_u can increase the magnetic resonance frequency, which is advantageous for the good permeability-frequency (μ - f) property in a high frequency region. However, the addition of Co to Fe-based amorphous alloys influences the crystallization process significantly. For example, it was recently reported that Cu clustering does not occur in a $(\text{Fe}_{0.5}\text{Co}_{0.5})_{88}\text{Zr}_7\text{B}_4\text{Cu}_1$ alloy,^{18,19} while Cu atoms form clusters in a $\text{Fe}_{88}\text{Zr}_7\text{B}_4\text{Cu}_1$ alloy prior to the crystallization.²⁰ Thus it is necessary to investigate the effect of Cu and Co on the microstructural evolution from (Fe,Co)–Si–B–Nb–Cu amorphous alloys to optimize the nanocrystalline microstructure for obtaining good soft magnetic properties in Co containing FINEMET type alloys.

^{a)} Author to whom correspondence should be addressed; electronic mail: ohnuma.masato@nims.go.jp

The aim of this study was to achieve low coercivity in Co-replaced FINEMET type alloys to improve the high frequency performance of Fe-based nanocrystalline softmagnetic materials. We have investigated the microstructural evolution by the crystallization of $\text{Fe}_{78.8-x}\text{Co}_x\text{Si}_9\text{B}_9\text{Nb}_{2.6}\text{Cu}_{0.6}$ ($x=0, 5, 20, 40,$ and 60) melt-spun amorphous ribbons by TEM and a three-dimensional atom-probe (3DAP) to optimize the nanocrystal/amorphous microstructure. In this work, we have clarified the influence of Co addition on the clustering behavior of Cu atoms and the final microstructure. Thermodynamical consideration was given to the interpretation on the microstructural change by Co addition, and we have proposed a new composition to achieve low coercivity with a Co content to enhance the high frequency property of FINEMET type alloys.

II. EXPERIMENT

Amorphous $\text{Fe}_{78.8-x}\text{Co}_x\text{Si}_9\text{B}_9\text{Nb}_{2.6}\text{Cu}_{0.6}$ ($x=0, 5, 20, 40,$ and 60) and $\text{Fe}_{39.4-y}\text{Co}_{40}\text{Si}_9\text{B}_9\text{Nb}_{2.6}\text{Cu}_y$ ($y=0.6, 1.0,$ and 1.5) alloy ribbons were prepared by the single roller melt-spinning technique. The thickness of the melt-spun ribbons was about $30 \mu\text{m}$. The amorphous state of the as-quenched sample was confirmed by x-ray diffraction (XRD) and TEM. These ribbon specimens were annealed at various temperatures in vacuum under helium atmosphere isothermally. The typical annealing condition was 803 K for 1 h. Differential scanning calorimetry (DSC) measurement was performed using a high-sensitive DSC (MAC Science DSC 3200). For atom-probe characterization, the ribbons were mechanically ground to thin square rods and then electropolished by a microelectropolishing technique to make field ion microscope (FIM) specimens. A locally built energy compensated three-dimensional atom probe (3DAP) equipped with a CAMECA optical tomographic atom-probe detector²¹ was employed for local compositional analysis with a near-atomic resolution. Transmission electron microscope (TEM) observations were carried out on a Philips CM200 TEM. The specimens for TEM observations were prepared by ion milling. dc B - H curve and permeability were measured with an automatic hysteresis loop tracer and an impedance gain phase analyzer, respectively. Quality factor Q which is defined as μ'/μ'' (μ' : real part, μ'' imaginary part of permeability) was used to evaluate the high frequency property. The induced magnetic anisotropy constant K_u was estimated from anisotropy field H_K . The free energy-concentration curves of the supercooled liquid phase for Fe-Cu and $(\text{Fe}_{1-x}\text{Co}_x)$ -Cu systems were calculated using the ThermoCalc system.²² The heats of mixing for Fe-Cu and Fe-Co systems were taken from the SSOL database (Scientific Group Thermodata Europe Solution database),²² while that for Co-Cu was taken from Ref. 23.

III. RESULTS

A. $\text{Fe}_{78.8-x}\text{Co}_x\text{Si}_9\text{B}_9\text{Nb}_{2.6}\text{Cu}_{0.6}$ ($x=0-60$) alloys

Figure 1 shows the saturation magnetic flux density (B_s), coercivity (H_c), and anisotropy constant (K_u) of $\text{Fe}_{78.8-x}\text{Co}_x\text{Si}_9\text{B}_9\text{Nb}_{2.6}\text{Cu}_{0.6}$ ($x=0-60$) alloys annealed at 803 K for 60 min. B_s does not change up to 40 at. % Co,

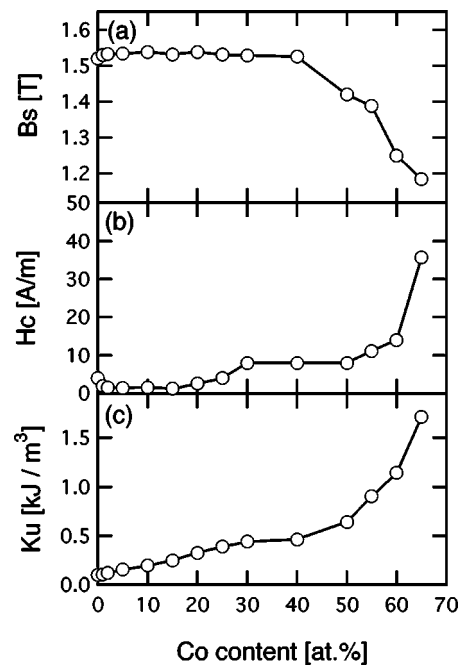


FIG. 1. Magnetic properties of $\text{Fe}_{78.8-x}\text{Co}_x\text{Si}_9\text{B}_9\text{Nb}_{2.6}\text{Cu}_{0.6}$ ($x=0-60$) alloys annealed at 803 K for 60 min. (a) Saturation magnetic flux density, B_s , (b) coercivity, H_c , and (c) anisotropy constant K_u vs Co concentration.

thereafter, it decreases as Co content increases. H_c does not change much below $x=20$, but it starts to increase when x becomes larger than 20. Above $x=50$, H_c increases drastically with Co content. K_u also increases monotonously and reaches a reasonably large value around $x=40$. Above $x=40$, K_u increases drastically with increasing x . Consequently, the resonance frequency which corresponds to the crossing point between the real part and the imaginary part of permeability, μ' and μ'' , respectively, shifts to a higher frequency range by substituting Fe with Co as shown in Fig. 2. Although the resonance frequency of the alloys with $x=40$ and $x=60$ is about 10 and more than 200 times larger than the alloy without Co, respectively, the permeability of the alloys decreases very much with increasing Co content because of the large H_c .

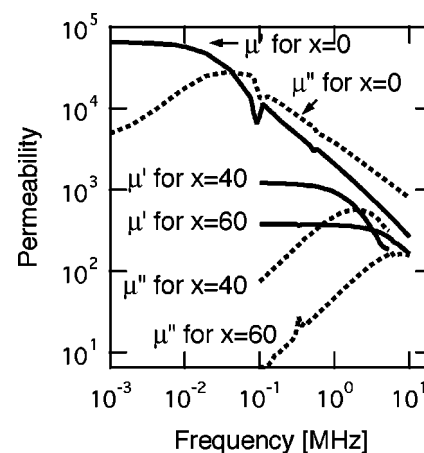


FIG. 2. Permeability of $\text{Fe}_{78.8-x}\text{Co}_x\text{Si}_9\text{B}_9\text{Nb}_{2.6}\text{Cu}_{0.6}$ ($x=0, 40,$ and 60) annealed at 803 K for 60 min vs Co concentration. μ' and μ'' are the real and imaginary parts of permeability, respectively.

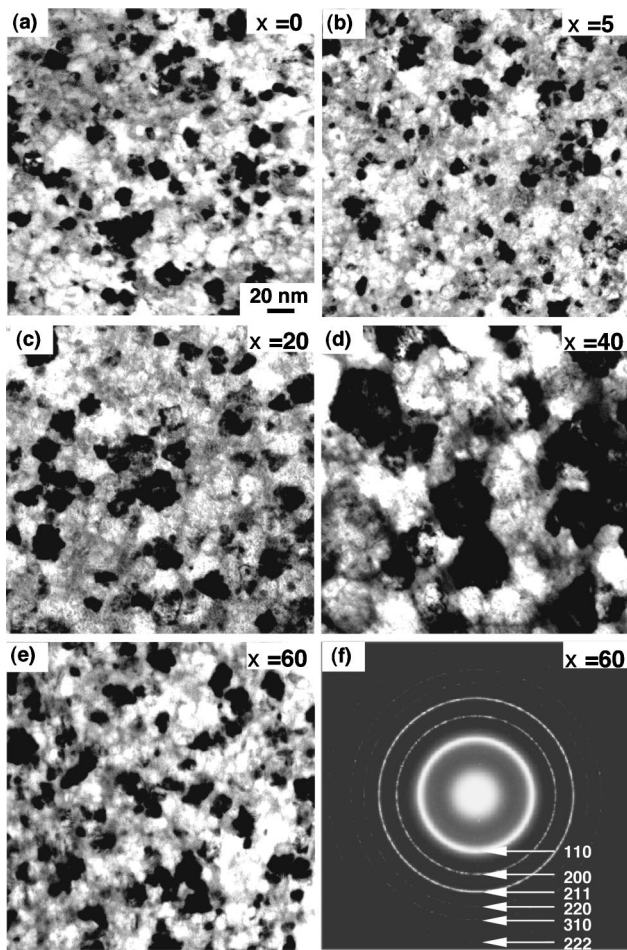


FIG. 3. TEM bright field micrographs of the $\text{Fe}_{78.8-x}\text{Co}_x\text{Si}_9\text{B}_9\text{Nb}_{2.6}\text{Cu}_{0.6}$ nanocrystalline samples with various Co contents [(a) $x=0$, (b) $x=5$, (c) $x=20$, (d) $x=40$, and (e) $x=60$] annealed at 803 K for 1 h. The selected area diffraction pattern of the 60 at. % Co-containing alloy annealed at 803 K for 1 h is shown in (f).

The microstructures have been studied by TEM to clarify the reason why H_c becomes large with x . Figure 3 shows TEM bright field micrographs of the $\text{Fe}_{78.8-x}\text{Co}_x\text{Si}_9\text{B}_9\text{Nb}_{2.6}\text{Cu}_{0.6}$ ($x=0, 5, 20, 40$, and 60) alloys annealed at 803 K for 1 h, a typical annealing condition for optimizing the soft magnetic properties. The constituent phases present in the above samples have been investigated by x-ray diffraction (XRD) and selected area electron diffraction (SAED). A bcc-FeCo(Si) phase and a residual amorphous phase were detected in all the specimens. One of the SAED patterns taken from the alloy with $x=60$ is shown in Fig. 3(f). A halo ring is observed at the position of d_{110} , suggesting the presence of the remaining amorphous phase. All rings are consistent with the bcc-FeCo(Si). Little difference in the average grain size (~ 15 nm) is observed between the samples with $x=0$ and $x=5$. In contrast, the samples with $x \geq 20$, whose coercivities are much higher than those for $x < 20$, has a much larger grain size, about 30 nm for $x=20$ [Fig. 3(c)] and 50 nm for $x=40$ [Fig. 3(d)]. Interestingly, the grain size reduces to 20 nm [Fig. 3(e)] in the alloy with $x=60$, while H_c of this alloy is large as shown in Fig. 1, indicating that the large H_c is not only because of the grain size.

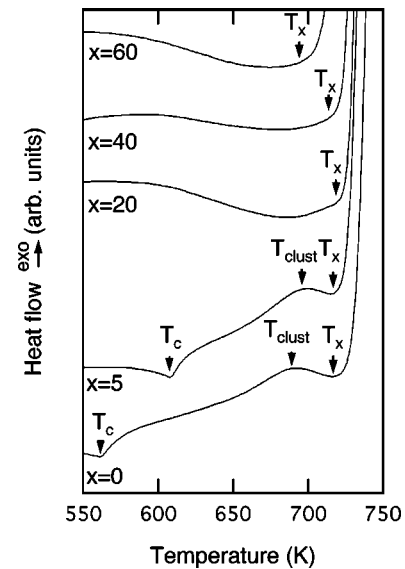


FIG. 4. DSC curves of $\text{Fe}_{78.8-x}\text{Co}_x\text{Si}_9\text{B}_9\text{Nb}_{2.6}\text{Cu}_{0.6}$ ($x=0, 5, 20, 40$, and 60) alloys at a heating rate of 0.33 K/s.

According to our previous study,¹⁰ the average grain size of the final microstructure is strongly influenced by the kinetics of the Cu clustering. For clarifying the change of the Cu clustering behavior with Co content, DSC curves of the $\text{Fe}_{78.8-x}\text{Co}_x\text{Si}_9\text{B}_9\text{Nb}_{2.6}\text{Cu}_{0.6}$ ($x=0, 5, 20, 40$, and 60) amorphous alloys were measured at a heating rate of 0.33 K/s. The substitution of Fe with Co increases the Currie temperature, T_c , as shown in Fig. 4, as expected from the Currie temperature change of Fe–Co binary alloys. T_c 's for the alloys with $x \geq 20$ are higher than the crystallization temperature (T_x) that appears as a sharp exothermic peak around 780 K. The small broad exothermic peaks between T_c and T_x for the samples with $x=0$ and 5 are attributed to the heat of Cu clustering, the peak position of which is defined as the clustering temperature, T_{clust} .¹⁰ T_{clust} shifts to a higher temperature after substituting Fe with 5 at. % Co. T_{clust} does not appear in the alloy with $x=20$ and 40 because T_{clust} becomes higher than T_x . These results indicate that Cu clustering occurs prior to the crystallization only in the alloys with $x \leq 5$ at a heating rate of 0.33 K/s.

The previous 3DAP investigation revealed that the fine grain size obtained in the FINEMET alloy is because of the formation of a high number density of Cu-enriched clusters ($\sim 10^{24} \text{ m}^{-3}$) that serve as heterogeneous nucleation sites for α -Fe particles.⁵ In order to observe how the number density of Cu-enriched clusters changes depending on the Co content, the distribution of Cu atoms was investigated by 3DAP. Figure 5 shows 3DAP Cu maps obtained from $\text{Fe}_{78.8-x}\text{Co}_x\text{Si}_9\text{B}_9\text{Nb}_{2.6}\text{Cu}_{0.6}$ ($x=0, 5, 20, 40$, and 60) alloys annealed at 803 K for 10 min, where each dot in the maps corresponds to one Cu atom. The sampling volume is about $10 \times 10 \times 50 \text{ nm}^3$. It is obvious that the density of Cu clusters decreases as the Co content increases. The estimated number density decreases from $2.0 \times 10^{24} \text{ m}^{-3}$ for $x=0$ to $3.0 \times 10^{23} \text{ m}^{-3}$ for $x=40$ as shown in Fig. 5. Although Cu clustering precedes the primary crystallization in the sample with $x < 20$, the bcc-FeCo(Si) phase was confirmed in the alloy

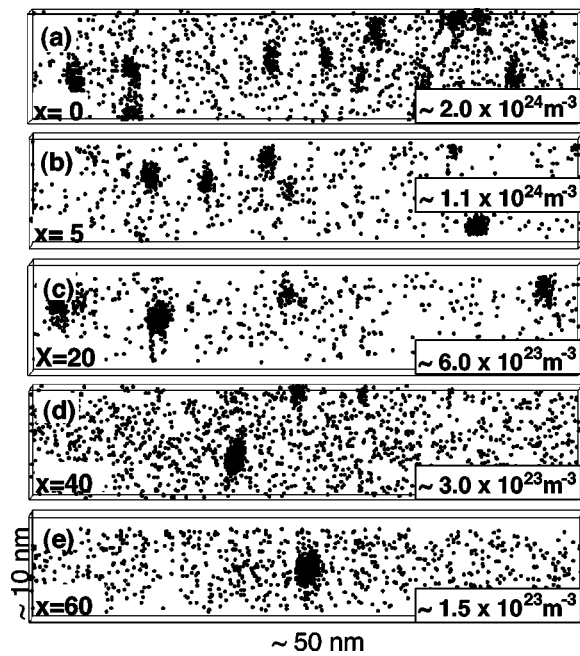


FIG. 5. 3DAP elemental mapping of Cu atoms obtained from the Fe_{78.8-x}Co_xSi₉B₉Nb_{2.6}Cu_{0.6} alloy annealed at 803 K for 10 min [(a) x=0, (b) x=5, (c) x=20, (d) x=40, and (e) x=60].

with $x \geq 20$ in this annealing condition, indicating that the Cu-enriched clusters form together with or after the nucleation of the bcc-FeCo(Si) primary crystals. These results indicate that the coarser grains in Co substituted alloys are attributed to the decrease or lack of the heterogeneous nucleation site for the primary crystals. Figure 5 also shows that the mechanism of the grain size refinement for the sample with $x = 60$ is not due to the presence of Cu clusters.

Figure 6 shows Cu concentration depth profiles of the Cu-enriched clusters observed in Fig. 5. As shown in this figure, the concentration of the Cu-enriched clusters in the alloys with $x \geq 20$ are much higher than those in the alloy with $x = 0$ or 5 in which Cu clustering occurs prior to the crystallization. The reason will be discussed using the CALPHAD method in the discussion section.

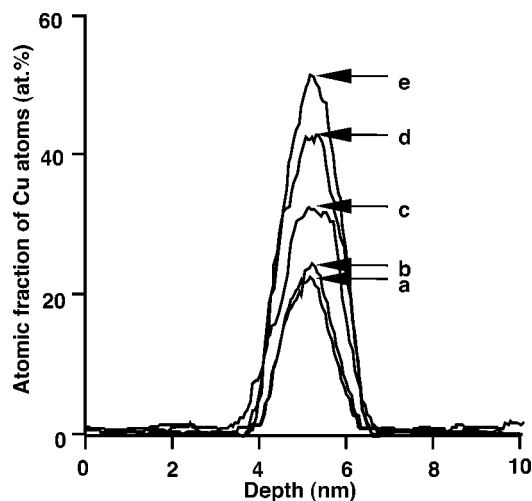


FIG. 6. Concentration depth profile of Cu for Cu clusters obtained from the Fe_{78.8-x}Co_xSi₉B₉Nb_{2.6}Cu_{0.6} alloy annealed at 803 K for 10 min [(a) x=0, (b) x=5, (c) x=20, (d) x=40, and (e) x=60].

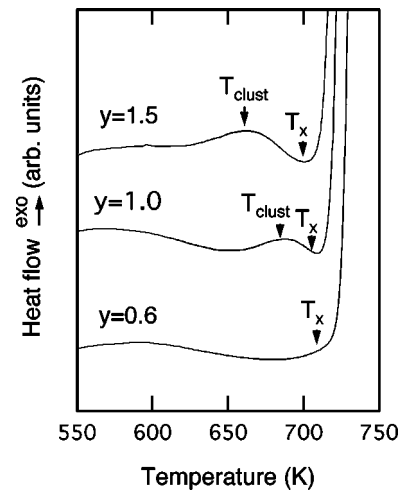


FIG. 7. DSC curves of Fe_{39.4-y}Co₄₀Si₉B₉Nb_{2.6}Cu_y (y=0.6, 1.0, and 1.5) alloys at a heating rate of 0.33 K/s.

B. Fe_{39.4-y}Co₄₀Si₉B₉Nb_{2.6}Cu_y (y=0.6, 1.0, and 1.5) alloys

Although K_u increases with Co content, x , the magnetic flux density, B_s , decreases drastically above $x = 50$ as shown in Fig. 1. The maximum concentration of Co in which Cu clustering can trigger the nucleation of primary crystals is $x = 40$ as described in the previous section. Thus there is a possibility to reduce the grain size further by enhancing the kinetics of the Cu clustering while maintaining reasonably large K_u and B_s in the alloy with $x = 40$. Therefore, the Cu content, y , of Fe_{39.4-y}Co₄₀Si₉B₉Nb_{2.6}Cu_y alloys ($x = 40$) was varied for optimizing the nanocrystalline microstructure. When y is increased, the kinetics for the Cu clustering is expected to become faster. Figure 7 shows the DSC curves of the samples with $y = 0.6, 1.0,$ and 1.5 . Only one prominent exothermic peak due to the primary crystallization of bcc-FeCo(Si) is detected in the alloy with $y = 0.6$ within the temperature range of the DSC measurement. In contrast, an additional broad and small exothermic peak corresponding to Cu clustering appears in the samples with $y = 1.0,$ and 1.5 . This result clearly indicates that the Cu clusters form prior to the crystallization in the alloys with $y \geq 1.0$, which can serve as heterogeneous nucleation sites for bcc-FeCo(Si). The peak position shifts to a lower temperature by increasing the Cu content as shown in Fig. 7 because the kinetics for the clustering become faster as y .

Figure 8 shows bright field TEM micrographs of the samples with (a) $y = 0.6,$ (b) $y = 1.0,$ and (c) $y = 1.5$ annealed at 803, 773, and 773 K for 1 h, respectively. Because the crystallization temperature decreases with increasing Cu content, lower annealing temperatures were chosen for the samples with higher Cu content. The grain size of the sample with $y = 1.0$ and 1.5 is significantly smaller than that with $y = 0.6$, indicating that the nanocrystallization occurred by the heterogeneous nucleation mechanism in the alloy with $y = 1.0$ and 1.5 .

Figure 9(a) shows the 3DAP map of B and Cu atoms in a small volume of approximately $5 \times 10 \times 50 \text{ nm}^3$. Cu atoms form a large number density of clusters, which is almost the

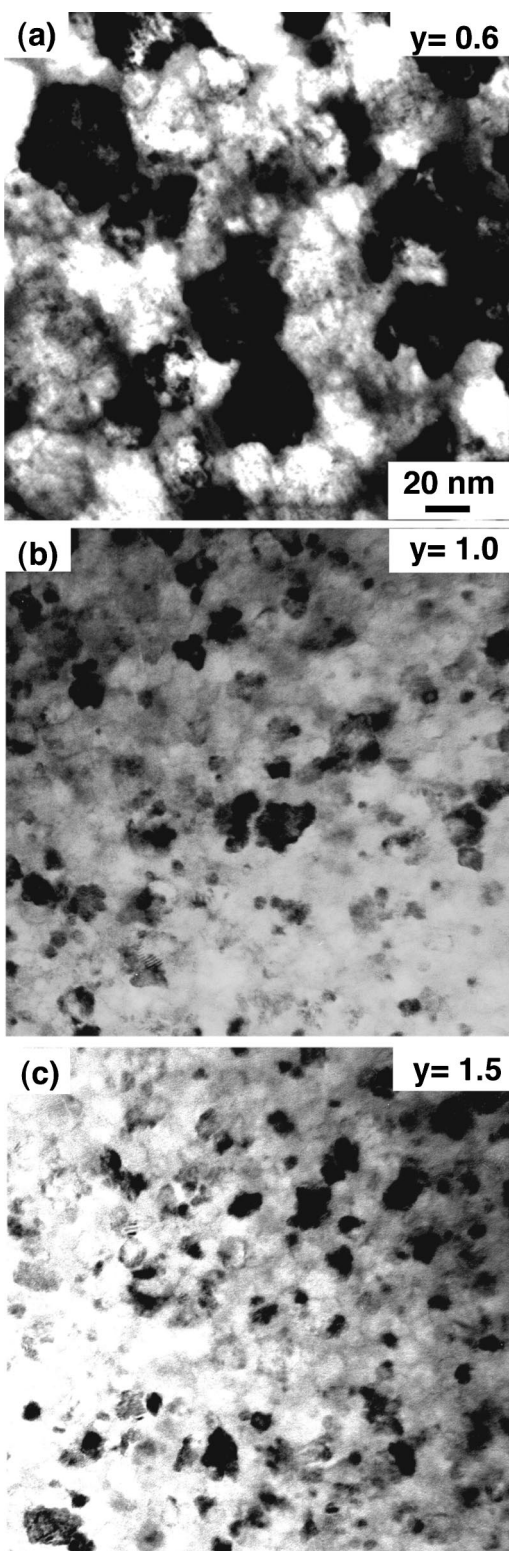


FIG. 8. TEM bright field micrographs of the $\text{Fe}_{39.4-y}\text{Co}_{40}\text{Si}_9\text{B}_9\text{Nb}_{2.6}\text{Cu}_y$ ($y=0.6, 1.0,$ and 1.5) alloys; (a) $y=0.6$ annealed at 803 K for 60 min, (b) $y=1.0$ annealed at 773 K for 60 min, and (c) $y=1.5$ annealed at 773 K for 60 min. Annealing temperatures are chosen from the peak broadening of x-ray diffraction measurements.

same order as that in the Co-free alloy [Fig. 5(a)]. As reported in the previous atom-probe work,⁵ B is enriched in the remaining amorphous phase. The B depleted region is bcc-FeCo. This phase may be ordered to the B2 structure, but

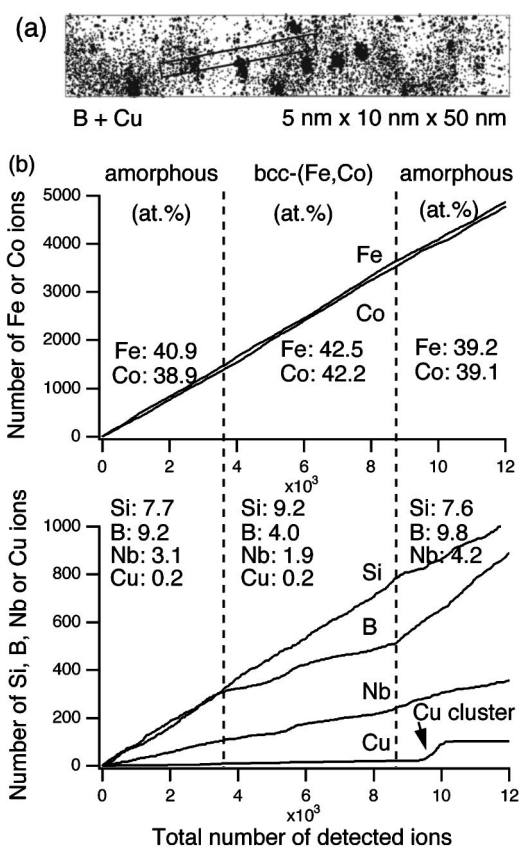


FIG. 9. (a) 3DAP elemental mapping of Cu and B atoms (sphere: Cu atom, dot: B atom) and (b) integrated concentration depth profile of constituent elements obtained from the $\text{Fe}_{38.4}\text{Co}_{40}\text{Si}_9\text{B}_9\text{Nb}_{2.6}\text{Cu}_{1.0}$ alloy annealed at 773 K for 60 min.

from the selected area electron diffraction pattern, the ordering cannot be detected due to the small difference in atomic scattering factors of Fe and Co. Figure 9(b) shows the integrated concentration depth profile measured from the volume containing a bcc-FeCo and the remaining amorphous phase. The composition of the bcc-FeCo is close to $\text{Fe}_{42}\text{Co}_{42}\text{Si}_9\text{B}_4\text{Nb}_2$. The remaining amorphous phase is close to $\text{Fe}_{39}\text{Co}_{39}\text{Si}_8\text{B}_{10}\text{Nb}_4$. The Fe/Co ratio in the bcc-FeCo is 1. Although Co and Si are slightly enriched in the bcc-FeCo phase, the partitioning tendency is very weak. Co is almost uniform in the alloy; Si is partitioned slightly in the bcc-FeCo. On the other hand, B and Nb are enriched in the remaining amorphous phase, but the partitioning tendency appears to be much weaker than that observed in the Co-free FINEMET alloy.⁵ Ping *et al.* reported that Co was preferentially partitioned in the remaining amorphous phase in a $\text{Fe}_{44}\text{Co}_{44}\text{Zr}_7\text{B}_4\text{Cu}_1$ (HITPERM) alloy, the Fe/Co ratio in the bcc-FeCo was determined to be 1.55.¹⁸ They attributed this to the high pair interaction between Co and Zr atoms. However, in the present alloy, Co is not partitioned in the remaining amorphous phase. This can be explained from the fact that the pair interaction between Co and Nb is not as high as that for CoZr. The predicted enthalpies of formation of CoZr and CoNb are -60 and -37 kJ/mol, respectively.²⁴ Because of the low pair interaction between Co and Nb with respect to Co and Zr, preferential partitioning of Co to the remaining amorphous phase does not occur in this alloy. The partition-

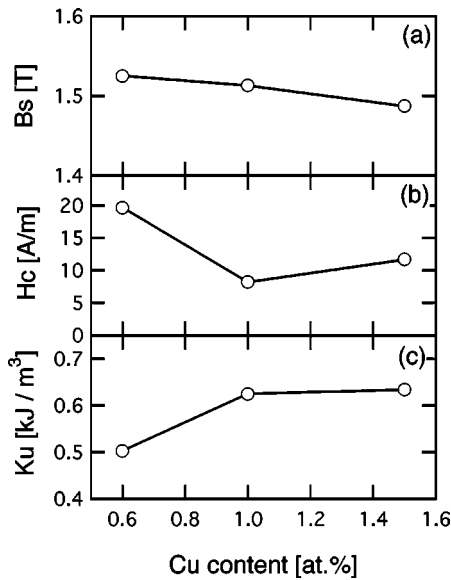


FIG. 10. Magnetic properties of $Fe_{39.4-y}Co_{40}Si_9B_9Nb_{2.6}Cu_y$ alloys annealed at 773 K for 60 min. (a) saturation magnetic flux density B_s , (b) coercivity H_c , and (c) anisotropy constant K_u vs Cu concentrations.

ing tendency of Si, B, and Nb also becomes weak in the Co substituted alloy.

Since the grain size refinement is achieved by increasing Cu, the H_c of the sample with $y=1$ is smaller than that of the alloy with $y=0.6$, while B_s decreases slightly with increasing y . However, the B_s is still larger than that of the sample with $x=50$, cf. Figs. 10(a) and 1(a). In addition, K_u for the samples with $y=1.0$ and 1.5 increases up to about $630 J/m^3$ after field annealing, which is almost the same level as that of the 50 at. % Co alloy, cf. Figs. 10(c) and 1(c). Figure 11(a) shows the μ - f curves for the alloy with $y=0.6$ and 1.0 . The resonance frequencies for the sample with $y=0.6$ and 1.0 are 2 and 5 MHz, respectively, namely, the resonance frequency increased more than double by optimizing the nanocrystalline size. In addition, μ'' for the sample with $y=1.0$ becomes lower than that of the sample with $y=0.6$. Consequently, the quality factor Q ($=\mu'/\mu''$) of the sample with $y=1.0$ is higher than that for $y=0.6$, indicating that the performance in the high frequency region is improved by increasing the Cu content from 0.6 to 1.0 at. %. These results have shown that the modified alloy has some advantage in the applications of high frequency range compared to the original FINEMET alloy.

IV. DISCUSSION

The previous 3DAP study has shown convincingly that the Cu clustering in FINEMET alloy occurs in the amorphous state prior to the primary crystallization of the bcc-Fe(Si) phase.⁵ This Cu clustering can be interpreted as the phase separation in the amorphous phase. In order to understand the thermodynamic driving force for the phase separation, the Gibbs free energy composition diagrams of supercooled liquid phase were calculated using the (calculation of the phase diagrams) CALPHAD method for Fe-Cu binary and (Fe,Co)-Cu pseudobinary alloys. Because of the lack of

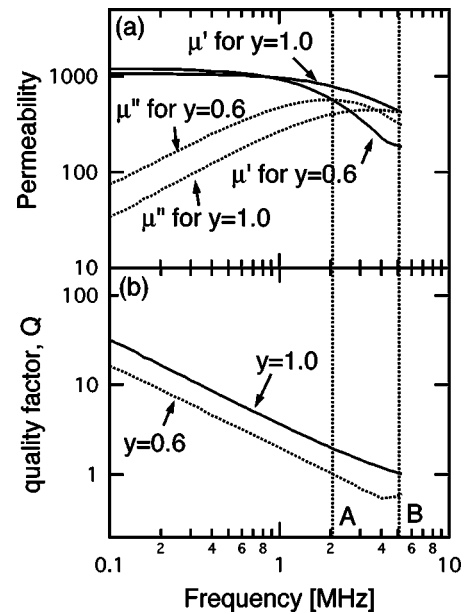


FIG. 11. (a) Permeability and (b) quality factor Q of $Fe_{39.4-y}Co_{40}Si_9B_9Nb_{2.6}Cu_y$ ($y=0.6$ and 1.0) alloys annealed at 773 K for 60 min vs frequency. Q is defined as μ'/μ'' where μ' and μ'' are the real and imaginary parts of permeability, respectively. The resonance frequency for $y=0.6$ and 1.0 alloy is indicated as lines A and B, respectively.

thermodynamic parameters for all possible combination of the constituent elements of the Fe-Si-B-Nb-Cu alloys, only the thermodynamic parameters among Fe, Co, and Cu were taken into account in the calculation of the free energy curves. We discuss the phase separation behavior in the amorphous phase of the present alloys based on the calculated free energy of the supercooled liquid phase. Thus the discussion given here will only explain the tendency of the thermodynamic driving force for the phase decomposition.

Figure 12 shows the free energy composition curves of the supercooled liquid phase for the $(Fe_{1-x}Co_x)$ -Cu system that were calculated using Thermo-Calc.²² The interaction parameters for Fe-Cu and Fe-Co in the SSOL database²² were used. Because the database does not have the parameter for Co-Cu, it was taken from Ref. 23. These free energy-concentration curves were calculated at 700 K where the Cu clustering was observed in the DSC measurements. The enthalpy term is dominant in the free energy at such a low temperature. Hence the free energy composition curves show two minima at the concentrations that are very close to both sides in Fig. 12 due to a large positive heat of mixing between Fe and Cu. The phase separation can occur in the supercooled liquid within A and B on the common tangent in Fig. 12. In the case of the nucleation and growth mechanism, the driving force for the formation of the Cu enriched phase can be evaluated from the difference in the free energy between B and D on the tangent line at concentration C. As shown in Fig. 11, it is clear that the driving force for the precipitation of the Cu enriched phase decreases from ~ 13 to ~ 10 kJ/mol with increasing Co content. This is the primary reason why the clustering temperature shifts to a higher temperature with increasing Co contents in the $Fe_{78.8-x}Co_xSi_9B_9Nb_{2.6}Cu_{0.6}$ alloys.

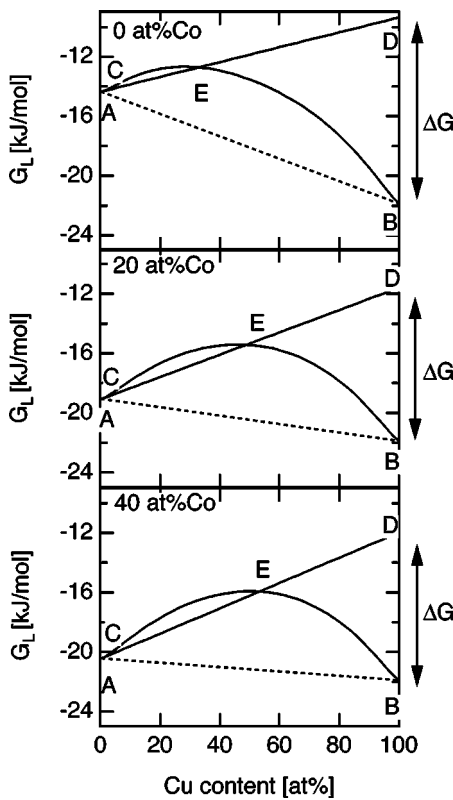


FIG. 12. Free energy-concentration curves of the supercooled liquid phase at 700 K for different Co/Fe ratios. The Co concentration shown in the inset corresponds to the concentrations in $Fe_{78.8-x}Co_xSi_9B_9Nb_{2.6}Cu_{0.6}$ alloys. The driving force of Cu clustering corresponds to the difference between B and D (the length of the arrow in the right side) for the alloy with 0, 20, and 40 at. % Co is ~ 13 , ~ 10 , and ~ 10 kJ/mol, respectively. A and B : the common tangent point, C : corresponds to the Cu composition which has the same ratio with that of $Fe_{78.8-x}Co_xSi_9B_9Nb_{2.6}Cu_{0.6}$, D : the value of the tangent line at the concentration which produces a common tangent at B, and E: crossing point between the tangent lines at C and the free energy curves.

The concentrations of Cu-enriched clusters measured by the 3DAP analysis in Fig. 6 are much lower than B, which is the equilibrium value for the Cu enriched amorphous phase (or Cu cluster). A possible interpretation for this observation is either the phase separation by the spinodal mechanism or the phase separation by clustering via an intermediate liquid phase. The spinodal mechanism, however, is unlikely because the Cu contents of the alloys in this study are out of the spinodal range as shown in Fig. 13, which was calculated from the inflection points of the free energy curves ($d^2G_L/dx^2=0$) calculated at several temperatures (not shown here). In contrast, as shown in Fig. 14, the intermediate liquid phase with the Cu concentration higher than the intersecting point, E, can form spontaneously because it decreases the free energy. The kinetics of clustering is controlled by both the thermodynamic driving force and the diffusion of solute atoms. The formation of the intermediate liquid phase with a lower Cu concentration requires less diffusion of Cu atoms than that of the equilibrium one (B in Fig. 12). Also, the interfacial energy of the clusters with a lower solute concentration must be smaller than those with the equilibrium concentration because the interfacial energy is proportional to the square of the concentration difference. Therefore the formation of Cu-enriched clusters with a lower

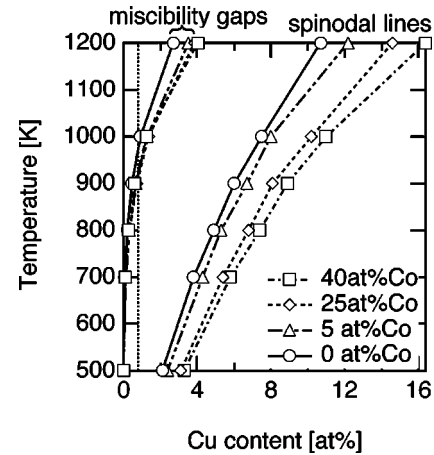


FIG. 13. Miscibility gaps and spinodal lines for the supercooled liquid phase for different Co/Fe ratios. The Co concentration shown in the inset corresponds to the concentrations in $Fe_{78.8-x}Co_xSi_9B_9Nb_{2.6}Cu_{0.6}$ alloys.

concentration than equilibrium B is probably favorable at the early stage of clustering. In fact, the bcc Cu precipitates with a substantially lower composition than the equilibrium value reported previously.²⁵ The present 3DAP results have also shown that the Cu concentrations in the observed clusters become higher with increasing Co content as shown in Fig. 6. This tendency can also be explained from the fact that the intersecting point E shifts to a higher Cu concentration with increasing Co content as shown in Fig. 12.

The Cu clustering does not occur prior to the crystallization when Co concentration is higher than 20 at. % as shown in Fig. 4. The Co concentration with Fe/Co close to one is desirable to apply high field-induced anisotropy to the alloys, since the induced anisotropy is expected to vary as $c^2(1-c)^2$, where c is the atomic fraction of A in a binary AB alloy, assuming that the anisotropy is due to an interaction between major constituents, namely Fe and Co.²⁶ Thus it is desirable to find a way to refine the crystallized microstructure of the alloy with $x \sim 40$ where the Fe/Co ratio is

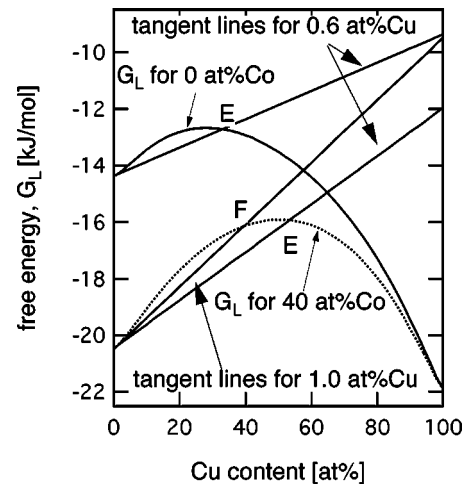


FIG. 14. Free energy curves for the supercooled liquid phase without Co and with 40 at. % Co at 700 K. E: crossing points between the tangent lines at 0.6 at. % Cu, and F: crossing points between the tangent lines at 1.0 at. % Cu and the free energy curves for 40 at. % Co.

almost one. Figure 13 shows the free-energy concentration diagram of the supercooled liquid at 700 K for Fe–Cu and Fe_{0.5}Co_{0.5}–Cu alloys which gives the same Fe/Co ratio with the 40 at. % Co alloy. The driving force for the Cu clustering in the alloys containing 0.6 at. % Cu is much lower in the Co containing alloy than that of the Co free alloy. However, the tangent line at 1.0 at. % Cu for the alloy with 40 at. % Co gives almost the same driving force for Cu clustering as that of the Co-free alloy containing 0.6 at. % Cu. The intersecting point, F , also shifts to lower Cu content which is almost the same as that of the Co-free alloy containing 0.6 at. % Cu. This suggests that higher Cu concentration is required to enhance the Cu clustering in the Co containing alloy. Based on this consideration, we measured the clustering and crystallization kinetics of Fe_{39.4–y}Co₄₀Si₉B₉Nb_{2.6}Cu_y alloys with $y=0.6, 1.0, \text{ and } 1.5$, and found that Cu clustering occurred prior to the crystallization when $y \geq 1.0$. The Cu concentration in the clusters becomes lower and the number density of Cu enriched clusters is increased by adding 1.0 at. % Cu to the alloy with 40 at. % Co as shown in Fig. 9. Consequently, the grain size is refined to approximately 10 nm, similar to the grain size of Co free alloys.

A similar effect of Co addition on the Cu clustering behavior was reported in other Fe-based nanocrystalline soft and hard magnetic materials such as Fe–Zr–B–Cu and Fe–Nd–B–Nb–Cu. No Cu cluster was detected in the (Fe_{0.5}Co_{0.5})₈₈Zr₇B₄Cu₁ alloy¹⁹ and Co-containing Fe_{76.5}Nd₈Co₈B₆Nb₁Cu_{0.2} nanocomposite hard magnetic alloys.²⁷ As long as the above discussion on the thermodynamic driving force for the formation of Cu clusters is valid for the multicomponent alloys, the same interpretation can be applied to these similar alloys.

In addition to the grain size refinement by the heterogeneous nucleation mechanism at the Cu-enriched clusters, there must be some other mechanism for the grain size refinement observed in the alloy with $x \geq 60$. To the authors' knowledge, in most of the amorphous alloys that show nanocrystallization without the heterogeneous nucleation mechanism, the heat of the mixing between the major constituents is large in negative value, i.e., Fe–Zr in the Fe–Zr–B system and Zr–Pd (Ref. 28) or many other Zr-based bulk metallic glasses. In the Co enriched alloy, the heat of mixing between Co and Nb falls in this category. When the ratio between Co/Fe exceeds one, this effect seems to become dominant. A detailed analysis for the local structure in atomic scale is required for clarifying the mechanism of nanocrystallization in these systems.

V. CONCLUSIONS

We have investigated the microstructures and the magnetic properties of Fe_{78.8–x}Co_xSi₉B₉Nb_{2.6}Cu_{0.6} ($x=0, 5, 20, 40, \text{ and } 60$) and Fe_{39.4–y}Co₄₀Si₉B₉Nb_{2.6}Cu_y ($y=0.6, 1.0, \text{ and } 1.5$) alloys in order to improve the high frequency soft magnetic properties of Fe–Si–B–Nb–Cu based nanocrystalline alloys, and the following conclusions were obtained.

(1) The permeability decreases and coercivity increases with Co content, x , because of the increase of the grain size.

(2) The grain size increase with x is attributed to the decrease of the number density of the Cu clusters that serve as heterogeneous nucleation sites for bcc-FeCo(Si) primary crystals, because the driving force for the Cu clustering decreases with increasing x .

(3) The decrease of the driving force for the Cu clustering in the Co-containing alloy was shown based on the free energy-concentration curves for the supercooled liquid phase in Fe–Cu and Fe_{1–x}Co_x–Cu model systems calculated by the CALPHAD method.

(4) The increase of Cu content, y , is effective in refining the crystallized microstructure of the alloy containing 40 at. % Co. It was confirmed that the Cu clustering occurred prior to the crystallization in the alloy with $x=40$ when $y \geq 1.0$. Consequently, the grain size decreased to about 10 nm, resulting in the low coercivity in an optimized alloy composition of Fe_{38.4}Co₄₀Si₉B₉Nb_{2.6}Cu_{1.0}.

(5) By this grain size refinement, the soft magnetic properties in the alloy with a higher Co concentration are significantly improved, to which a higher magnetic anisotropy can be induced by magnetic annealing. The coercivity, permeability and resonance frequency of the new alloy composition is suitable for applications in a higher frequency range (5 MHz).

ACKNOWLEDGMENT

This work was supported by the Special Coordination Funds for Promoting Science and Technology on "Nanohetero Metallic Materials" from the Ministry of Education, Sports, Culture, Science and Technology.

- ¹Y. Yoshizawa, S. Oguma, and K. Yamauchi, *J. Appl. Phys.* **64**, 6044 (1988).
- ²G. Herzer, *IEEE Trans. Magn.* **25**, 3327 (1989).
- ³K. Hono, K. Hiraga, Q. Wang, A. Inoue, and T. Sakurai, *Acta Metall. Mater.* **40**, 2137 (1992).
- ⁴K. Hono, Y. Zhang, A. Inoue, and T. Sakurai, *Mater. Trans., JIM* **36**, 909 (1995).
- ⁵K. Hono, D. H. Ping, M. Ohnuma, and H. Onodera, *Acta Mater.* **47**, 997 (1999).
- ⁶J. D. Ayers, V. G. Harris, J. A. Sprague, W. T. Elam, and H. N. Jones, *Acta Metall. Mater.* **46**, 1861 (1998).
- ⁷J. D. Ayers, V. G. Harris, J. A. Sprague, and W. T. Elam, *Appl. Phys. Lett.* **64**, 974 (1994).
- ⁸T. Pradell, J. Zhu, N. Claveguera, and M. T. Claveguera-Mora, *J. Appl. Phys.* **83**, 5171 (1998).
- ⁹M. Ohnuma, K. Hono, H. Onodera, J. S. Pedersen, and S. Linderoth, *Nanostruct. Mater.* **12**, 693 (1999).
- ¹⁰M. Ohnuma, K. Hono, S. Linderoth, J. S. Pedersen, Y. Yoshizawa, and H. Onodera, *Acta Mater.* **48**, 4783 (2000).
- ¹¹A. Danzig, A. Wiedenmann, and N. Mattern, *Physica B* **234**, 611 (1997).
- ¹²J. Kohlbrecher, A. Wiedenmann, and H. Wollenberger, *Physica B* **213**, 579 (1995).
- ¹³G. Rixecker, P. Schaaf, and U. Gonser, *J. Phys.: Condens. Matter* **4**, 10295 (1992).
- ¹⁴Y. Zhang, K. Hono, A. Inoue, and T. Sakurai, *Scr. Mater.* **34**, 1705 (1996).
- ¹⁵D. H. Ping, K. Hono, H. Kanekiyo, and S. Hirosawa, *Acta Metall. Mater.* **47**, 4641 (1999).
- ¹⁶M. Müller, H. Grahl, N. Mattern, U. Kuhn, and B. Schnell, *J. Magn. Magn. Mater.* **160**, 284 (1996).
- ¹⁷H. Fujimori, H. Morita, Y. Obi, and S. Ohta, in *Amorphous Magnetism II 1977*, edited by R. A. Levy and R. Hasegawa (Plenum, New York, 1977), p. 393.
- ¹⁸D. H. Ping, Y. Q. Wu, K. Hono, M. A. Willard, M. E. McHenry, and D. E. Laughlin, *Scr. Mater.* **45**, 781 (2001).

- ¹⁹M. A. Willard, M. Q. Huang, D. E. Laughlin, M. E. McHenry, J. O. Cross, and V. G. Harris, *J. Appl. Phys.* **85**, 4421 (1999).
- ²⁰T. Ohkubo, H. Kai, D. H. Ping, K. Hono, and Y. Hirotsu, *Scr. Mater.* **44**, 971 (2001).
- ²¹B. Deconihout, L. Renaud, G. Da Costa, M. Bouet, A. Bostel, and D. Blavette, *Ultramicroscopy* **73**, 253 (1998).
- ²²B. Sundman, B. Jansson, and J-O. Andersson, *CALPHAD: Comput. Coupling Phase Diagrams Thermochem.* **9**, 153 (1985).
- ²³M. Hasebe, K. Oikawa, and T. Nishizawa, *J. Jpn. Inst. Met.* **46**, 584 (1982).
- ²⁴F. R. de Boer, R. Boom, W. C. M. Mattens, A. R. Miedema, and A. K. Niessen, *Cohesion in Metals: Transition Metal Alloys* (North-Holland, Amsterdam, 1989).
- ²⁵S. R. Goodman, S. S. Brenner, and J. R. Low, *Metall. Trans.* **4**, 2371 (1973).
- ²⁶S. Chikazumi and T. Oomura, *J. Phys. Soc. Jpn.* **10**, 842 (1955).
- ²⁷Y. Q. Wu, D. H. Ping, K. Hono, M. Hamano, and A. Inoue, *J. Appl. Phys.* **87**, 8658 (2000).
- ²⁸C. Fan and A. Inoue, *Mater. Trans., JIM* **38**, 1040 (1997).